



Cite this: *Chem. Sci.*, 2024, 15, 17663

All publication charges for this article have been paid for by the Royal Society of Chemistry

# Enhanced chiroptical activity for narrow deep-blue emission in axial chiral frameworks *via* three-dimensional interlocking†

Xuechao Mo, Guohao Chen, Yulan Li, Biao Xiao, Xuefeng Chen, Xiaojun Yin \* and Chuluo Yang 

The advancement of desirable circularly polarized luminescence (CPL) emitters is predominantly constrained by the effective regulation of magnetic and electric transition vectors, particularly within the deep-blue spectral domain. Herein, we present four pairs of novel chiral emitters with systematically varied molecular rigidity, symmetry, and chiral centers to elucidate the intrinsic coupling of key molecular parameters influencing their chiroptical properties. Notably, the incorporation of appropriate intramolecular 3D-interlocking within a natural binaphthyl chirality skeleton offers an effective approach to achieving both significantly narrowed full width at half maximum (FWHM, as low as 18 nm) and substantially enhanced chiroptical activity (luminous dissymmetry factor,  $g_{PL}$ , up to  $3.0 \times 10^{-3}$ ). Additionally, introducing a secondary chiral center closely parallel to the primary chiral plane facilitates strong chiral–chiral interactions, further affording a 50% improvement in their  $g_{PL}$  values. As a demonstration, vacuum-deposited circularly polarized organic light-emitting diodes incorporating these pure fluorescent emitters exhibit outstanding electroluminescent performance, with maximum external quantum efficiency exceeding 5.35%, favorable FWHM of approximately 25 nm, and extreme CIE<sub>y</sub> values below 0.03.

Received 29th July 2024  
Accepted 4th October 2024

DOI: 10.1039/d4sc05056h  
rsc.li/chemical-science

## Introduction

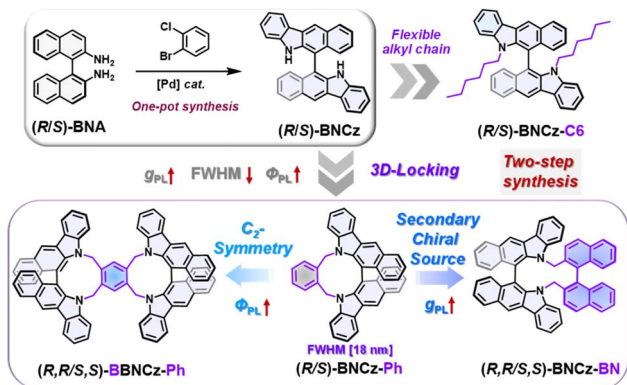
Circularly polarized luminophores (CPL) capable of emitting circularly polarized light directly circumvent the necessity for intricate chiral transfer processes or supplementary optical components,<sup>1</sup> hold promise for integration into next-generation optoelectronic applications,<sup>2</sup> such as optical information encryption,<sup>3</sup> chiral sensing,<sup>4</sup> and three-dimensional displays.<sup>5</sup> The simultaneous achievement of both high luminous dissymmetry factor ( $g_{PL}$ ) and fluorescence quantum yield delineates the ongoing quest for ideal CPLs, necessitating the presence of partially allowed magnetic and electric transition moments aligned in precise orientations.<sup>6</sup> However, for conjugated pure organic emitters, the radiative transition process typically involves only  $\pi^*-\pi$  or charge-transfer transitions, which are often magnetically forbidden, resulting in low  $g_{PL}$  values ranging from  $10^{-5}$  to  $10^{-3}$ .<sup>7</sup> Despite the observation of exceptional  $g_{PL}$  values exceeding  $10^{-2}$  through self-assembly

into long-range ordered liquid crystalline phases or nano-wires,<sup>8</sup> such configurations are incompatible with the manufacturing processes of state-of-the-art electronic devices.<sup>9</sup> The advancements in creating new chiral donors/acceptors or diverse screw-shaped  $\pi$ -extended topological structures offer opportunities to generate promising chiral emitters with competitive  $g_{PL}$  values,<sup>10</sup> attributed to the significant engagement of chiral centers in radiative excited states.<sup>11</sup> Additionally, endeavors to disentangle the intricate interplay between magnetic and electric transition moments are increasingly emphasized.<sup>12</sup>

Owing to their inherent chiral donor characteristics, ease of modification, and avoidance of expensive chiral resolution processes, [1,1'-binaphthalene]-2,2'-diamine (BNA) and its derivatives exhibiting natural axis chirality find widespread utilization as chiral emitters for high-performance organic light emitting diodes (OLEDs).<sup>13</sup> For instance, Chen *et al.* exemplify the synthesis of deep-red thermal activation delayed fluorescence molecules (emission peak,  $\lambda_{em} = 660$  nm) through the integration of BNA with a potent acceptor, cyano-substituted phenopyrazine, resulting in a  $g_{PL}$  of  $1.7 \times 10^{-3}$  and a maximum external quantum efficiency ( $\eta_{EQE,max}$ ) of 6.2%.<sup>14</sup> Zheng and colleagues present a versatile approach to enhance the  $g_{PL}$  to  $5.3 \times 10^{-3}$  by incorporating the BNA donor onto the weak *ortho*-phthalonitrile acceptor, yielding both sky-blue emission ( $\lambda_{em} = 477$  nm) and an improved  $\eta_{EQE,max}$  of

Shenzhen Key Laboratory of New Information Display and Storage Materials, College of Materials Science and Engineering, Shenzhen University, Shenzhen, 518060, P. R. China. E-mail: xiaojunyin@szu.edu.cn; clyang@szu.edu.cn

† Electronic supplementary information (ESI) available: Detail synthesis and characterization, general information, photophysical, thermal and electrical properties of the chiral emitters, theoretical calculations, and crystal structures. CCDC 2372805–2372808. For ESI and crystallographic data in CIF or other electronic format see DOI: <https://doi.org/10.1039/d4sc05056h>



Scheme 1 Chemical structures and the molecular design concepts of the four pairs of deep-blue enantiomers.

20.5%.<sup>13c</sup> Our research group has recently proposed a dual-pronged strategy to reconcile the trade-offs between luminous efficiency and  $g_{PL}$  by directly fusing a secondary chiral donor (BNA) onto the multiple resonance (MR) scaffold, resulting in narrow-band pure-green emission along with a substantial  $g_{PL}$  ( $3.3 \times 10^{-3}$ ) and  $\eta_{EQE,max}$  of 36.1%.<sup>15</sup> Despite this, the availability of reliable CPL emitters in the deep-blue range and comprehensive studies elucidating factors crucial for determining their chiroptical properties,<sup>16</sup> such as configurational stability, molecular symmetry, and chiral–chiral interactions, remains notably limited, yet pivotal for further advancements toward high-quality CPLs.

In this study, four pairs of enantiomers based on BNA backbone with varying molecular rigidity, symmetry, and chiral centers were meticulously designed to elucidate the intrinsic coupling of key molecular parameters involved in chiroptical properties (Scheme 1). Remarkably, all these chiral emitters were synthesized *via* a straightforward two-step process (Scheme S1†) without requiring additional chiral resolution. Steady-state fluorescence measurements revealed that all these CPLs exhibited bright deep-blue emission with peaks around 416 nm, while the shape and full width at half maximum (FWHM) were significantly influenced by the spatial structure of the frameworks. Compared to the flexible *R/S*-BNCz-C6, the FWHM of *R/S*-BNCz-Ph with rigid 3D-interlocking structure was significantly narrowed to 18 nm, attributed to the hybrid localized  $\pi$ -bonding,

short-range charge transfer excitation characteristics, as well as reduced vibrational relaxation in the excited states. Additionally, a rigid geometry was essential for maintaining consistent vectors of both electric and magnetic transitions, resulting in more robust chiroptical properties for *R/S*-BNCz-Ph ( $1.1 \times 10^{-3}$ ) compared to *R/S*-BNCz-C6 ( $<1.0 \times 10^{-4}$ ). Furthermore, introducing a secondary chiral motif closely parallel to the primary chiral plane afforded potential chiral–chiral interactions, improving the  $g_{PL}$  value by 50% to  $1.6 \times 10^{-3}$ . Whereas, incorporating a repeating chiral BNCz with  $C_2$ -symmetry geometry led to an unfavorable vector angle and a decreased  $g_{PL}$  of  $0.6 \times 10^{-3}$ , but raised fluorescence quantum yield up to 0.92. Theoretical simulations and single-crystal analysis elucidated the key parameters influencing these differentiated chiroptical properties. As a demonstration, vacuum-evaporated OLEDs using these chiral emitters as emitting layers were fabricated, achieving favorable device performances with the maximum external quantum efficiency ( $\eta_{EQE,max}$ ) values all exceeding 4.00% (peaking at 5.35%) and desirable Commission Internationale de L'Eclairage (CIE) y-coordinates ( $CIE_y < 0.05$ ) conforming to the Broadcast Service Television 2020 (BT.2020) standard for blue emitters, representing one of the best results among pure fluorescence blue-OLEDs.

## Results and discussion

The detailed synthetic routes of these chiral emitters were outlined in Scheme S1,† involving a one-pot palladium-catalyzed Buchwald–Hartwig cross-coupling and oxidative coupling to yield the key intermediate *R/S*-BNCz, followed by nucleophilic substitution to produce the target compounds with substantial yields. All four pairs of chiral enantiomer emitters and key intermediates were comprehensively characterized using  $^1H$  and  $^{13}C$  nuclear magnetic resonance (Fig. S1–S8†) and high-resolution mass spectrometry. Notably, due to the 3D-locked steric configurations and shielding effect, the chemical shifts of the methylene group protons associated with the nitrogen atoms were distinctly split into two sets of doublet peaks (Fig. S3, S5 and S7†), reflecting a more rigid geometry in these intramolecular interlocking molecules in contrast to the open-ended manner (*R/S*-BNCz-C6, Fig. S2†). Thermogravimetric analysis confirmed the favorable thermal stability of these axially chiral compounds, with decomposition

Table 1 Photophysical, electrochemical and transient spectra data of these pairs of enantiomers

Emitters	$\lambda_{abs}^a$ [nm]	$\lambda_{em}^a$ [nm]	FWHM <sup>a</sup> [nm]	$E_{HOMO}/E_{LUMO}^b$ [eV]	$E_g^c$ [eV]	$\tau_p^d$ [ns]	$\Phi_{PL}^e$ [%]	$k_{r,s}^f$ [ $10^7$ s <sup>-1</sup> ]	$k_{nr,s}^f$ [ $10^7$ s <sup>-1</sup> ]	$g_{PL}^g$ [ $\times 10^{-3}$ ]
<i>R/S</i> -BNCz-C6	299, 321, 410	420	36	−5.34/−2.36	2.98	20.16	58	6.13	4.21	$<\pm 0.1$
<i>R/S</i> -BNCz-Ph	292, 322, 404	416	18	−5.32/−2.35	2.97	10.21	72	7.06	2.75	$\pm 1.1/\pm 3.0$
<i>R,R,S,S</i> -BBNCz-Ph	290, 322, 405	416	19	−5.30/−2.33	2.97	10.21	92	9.02	0.78	$\pm 0.6/\pm 0.8$
<i>R,R,S,S</i> -BNCz-BN	293, 387, 409	419	22	−5.22/−2.27	2.95	10.19	64	6.27	3.53	$\pm 1.6/\pm 1.5$

<sup>a</sup> The characteristic absorption peaks, emission peaks and full widths at half maximum were obtained in dilute toluene ( $1 \times 10^{-5}$  mol L<sup>-1</sup>).

<sup>b</sup>  $E_{HOMO}$  was evaluated from the half-wave potential of oxidation process of cyclic voltammetry curves with reference to the internal standard of ferrocene,  $E_{LUMO}$  was deduced by  $E_{HOMO}$  and optical gap. <sup>c</sup> Calculated from the onset of absorption spectra at long wavelength side.

<sup>d</sup> Obtained from the transient PL decay curves. <sup>e</sup> The total  $\Phi_{PL}$  was measured in 20 wt% doped thin films (in *mCBP*:*DBFPO* matrix, 1:1) under an argon atmosphere. <sup>f</sup> The rate constants involving in fluorescence radiative decay process were deduced by  $k_{r,s} = \Phi_{PL}/\tau_p$ ,  $k_{nr,s} = [(1 - \Phi_{PL})/\Phi_{PL}]k_{r,s}$ . <sup>g</sup> The  $g_{PL}$  values were obtained from CPPL spectra in dilute toluene or doped films.



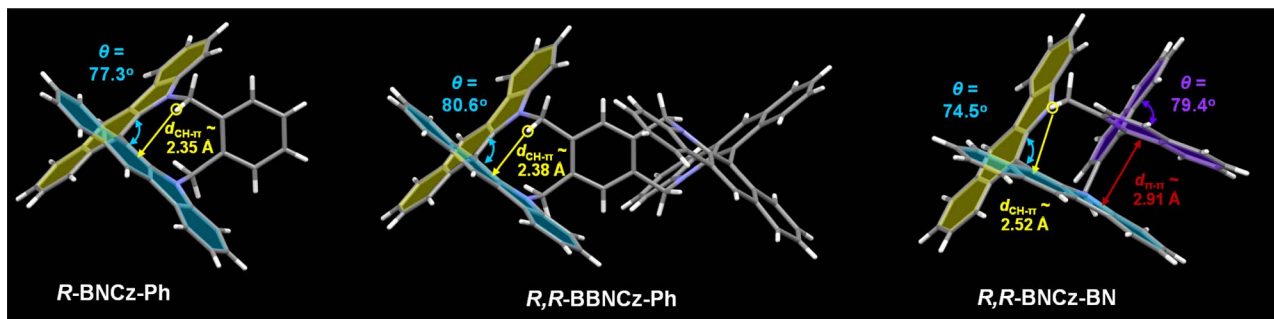


Fig. 1 The single-crystal structures of *R*-BNCz-Ph, *R,R*-BBNCz-Ph, and *R,R*-BNCz-BN.

temperatures ( $T_d$ , corresponding to 5% weight loss) all exceeding 386 °C (Fig. S9†). Cyclic voltammetry curves measured in dilute dichloromethane demonstrated a quasi-reversible oxidation process with observed half-wave potentials of 1.10, 1.08, and 0.99 V (vs. Ag/AgCl) for *R*-BNCz-Ph, *R,R*-BBNCz-Ph, and *R,R*-BNCz-BN, respectively. Accordingly, their HOMO levels ( $E_{\text{HOMOs}}$ ) were estimated to be  $-5.32$ ,  $-5.30$ , and  $-5.22$  eV, respectively (Table 1), with the distinctly elevated  $E_{\text{HOMOs}}$  of the latter attributed to the incorporated binaphthyl, which facilitated more effective  $\pi$ - $\pi$  interactions and enhanced  $\pi$ -delocalization. The single crystals of these 3D-locked chiral molecules were successfully obtained by the slow evaporation of their corresponding methanol/dichloromethane mixed solutions, with all resolved absolute structures aligning with our initial presumption. As depicted in Fig. 1 and S9†, the three chiral molecules exhibited highly twisted configurations with

near-vertical dihedral angles ( $75^\circ$  to  $80^\circ$ ) between the two 5*H*-benzo[*b*]carbazole (BCz) planes, attributed to the inserted large steric linking moieties. The measured CH- $\pi$  distances ( $d_{\text{CH}-\pi}$ ) between the BCz plane and the shielded hydrogen of methylene were approximately 2.36 Å for both *R*-BNCz-Ph and *R,R*-BBNCz-Ph, and slightly extended to 2.52 Å for *R,R*-BNCz-BN, consistent with the  $^1\text{H}$ -NMR results, providing additional interaction forces to restrict methylene rotation. Unlike the single phenyl plane, the incorporated chiral binaphthalene in *R,R*-BNCz-BN led to an orthogonal arrangement framework with a close  $d$ -spacing of approximately 2.91 Å between the BCz and naphthalene planes, offering sufficient distance to induce strong  $\pi$ - $\pi$  or chiral-chiral interactions, thereby enhancing their chiroptical properties.

The photophysical properties of these chiral emitters were examined in either dilute toluene solution ( $1 \times 10^{-5}$  M) or

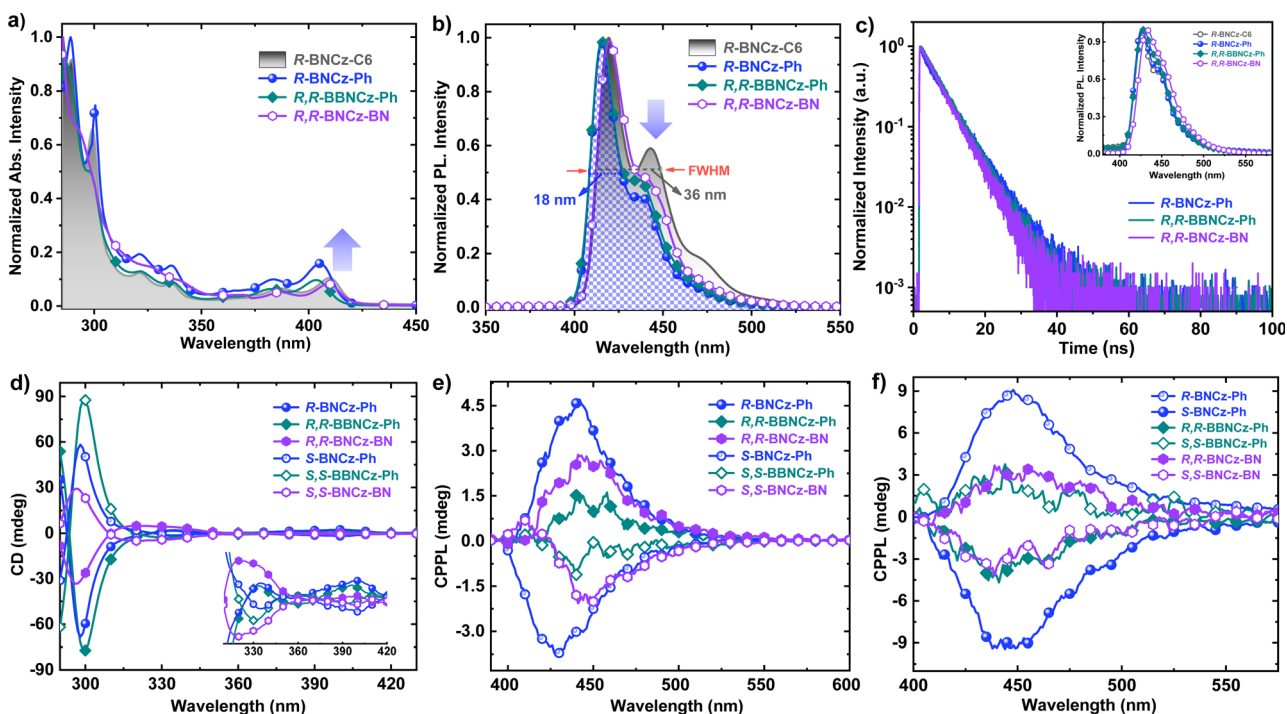


Fig. 2 The (a) UV-Vis absorption and (b) fluorescence spectra of *R*-BNCz-C6, *R*-BNCz-Ph, *R,R*-BBNCz-Ph and *R,R*-BNCz-BN in dilute toluene ( $1 \times 10^{-5}$  M), (c) transient PL spectra of these chiral emitters doped in *m*CBP : DBFO (1 : 1) matrix (inset: corresponding steady-state fluorescence spectra) the (d) CD, (e) CPPL spectra of these enantiomers in dilute toluene ( $1.0 \times 10^{-5}$  M) or (f) CPPL spectra in doped thin films.





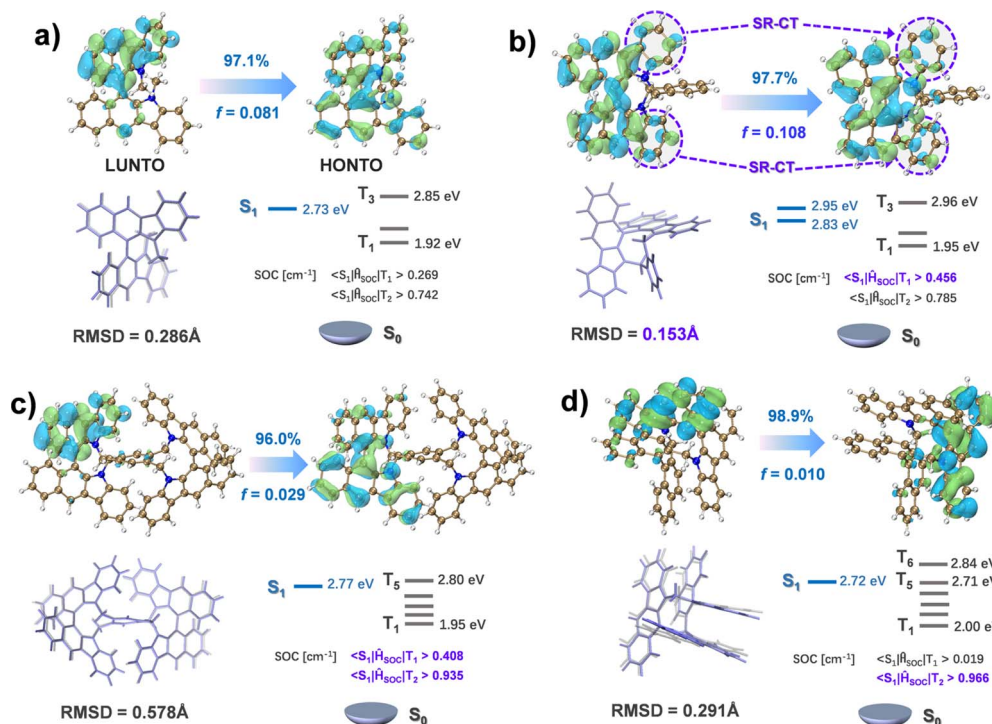


Fig. 3 The NTO analysis, structural difference between the optimized  $S_1$  (light purple) and  $S_0$  (gray), calculated key excited energy levels and relevant SOC values for (a)  $R$ -BNCz-C6, (b)  $R$ -BNCz-Ph, (c)  $R,R$ -BBNCz-Ph and (d)  $R,R$ -BNCz-BN.

doped thin films (20 wt% in **DBFPO** : **mCBP** matrix, 1 : 1), with the results presented in Fig. 2a–c and Table 1. As anticipated, all compounds exhibited intense  $\pi$ – $\pi^*$  transitions around 300 nm and relatively weaker  $n$ – $\pi^*$  transition bands around 380 nm. Additionally, a distinct absorption band over 400 nm was observed in all four emitters, belonging to the characteristic short-range charge-transfer (SR-CT) transition between adjacent atoms with differing electronegativities (Fig. 2a). Notably, compared to the rotatable **R-BNCz-C6**, the shoulder emission peaks of the other three with 3D-interlocked architectures were significantly weakened (Fig. 2b), resulting in a pronounced narrowing of the full width at half maximum (FWHM) from 36 nm to 18 nm (for **R-BNCz-Ph**). Such variation can be attributed to the enhanced molecular rigidity, which facilitated to suppress most vibrational and rotational modes, aligning with the intensified SR-CT observed in **R-BNCz-Ph** as well. Conversely, all four emitters exhibited similar narrow-band emission spectra in doped thin films (inset of Fig. 2c) due to the considerable restriction of molecular relaxation in the aggregate state. Interestingly, **R,R-BBNCz-Ph**, with its dual fluorescence centers and improved molecular symmetry, displayed a significantly enhanced photoluminescence quantum yield (PLQY, 0.92) compared to the single-center **R-BNCz-Ph** (0.72). Transient PL spectra recorded in the **mCBP** : **DBFPO** hybrid matrix showed monoexponential decay profiles for all samples (Fig. S13†), with fitted fluorescence lifetimes ( $\tau_f$ ) of approximately 10.2 ns. Additionally, the estimated energy gaps ( $\Delta E_{ST}$ ) between the lowest triplet ( $T_1$ ) and singlet ( $S_1$ ) states exceeded 0.48 eV (Fig. S11†), suggesting that the reverse

intersystem crossing (RISC) process from  $T_1$  to  $S_1$  is negligible. Furthermore, solvent polarity ( $f$ )-dependent absorption and fluorescence spectra (Fig. S12†) showed minimal Stokes shifts across varying  $f$ , aligning with typical radiative transitions dominated by local excitation mechanisms.

The chiroptical properties of these axial chirality emitters were investigated in both dilute toluene solutions and doped thin films as well. As shown in Fig. 2d and S14,† all samples exhibited characteristic mirror-symmetric circular dichroism (CD) signals with distinct wavy Cotton effects ranging from 280 nm to approximately 420 nm. Notably, all enantiomers displayed intense CD signals concentrated around 300 nm, attributed to the typical  $\pi$ -bonding type local excitation of BNCz segments. The relative strength of CD signals at longer wavelengths was notably enhanced with the introduction of a secondary chiral motif, which can be attributed to potential chiral–chiral interactions between the two interpenetrated chiral centers. Accordingly, the circularly polarized photoluminescence (CPPL) spectra and estimated  $g_{\text{PL}}$  values of both **R/S-BNCz-Ph** and **R,R/S,S-BNCz-BN** were significantly higher than those of **R,R/S,S-BBNCz-Ph**, due to the substantial contribution of SR-CT components or broadened  $\pi^*$ – $\pi$  transitions in the radiative  $S_1$  state. Interestingly, compared to the **R/S-BNCz-Ph** pair, the **R,R/S,S-BNCz-BN**, with its two chiral centers and mutually orthogonal molecular configuration, showed a 50% improvement in  $g_{\text{PL}}$  values (i.e.,  $1.6 \times 10^{-3}$  vs.  $1.1 \times 10^{-3}$ ), as elucidated by following theoretical calculations. However, in the aggregate state, such trend was slightly reversed, with the chiroptical features of **R/S-BNCz-Ph** being remarkably superior to



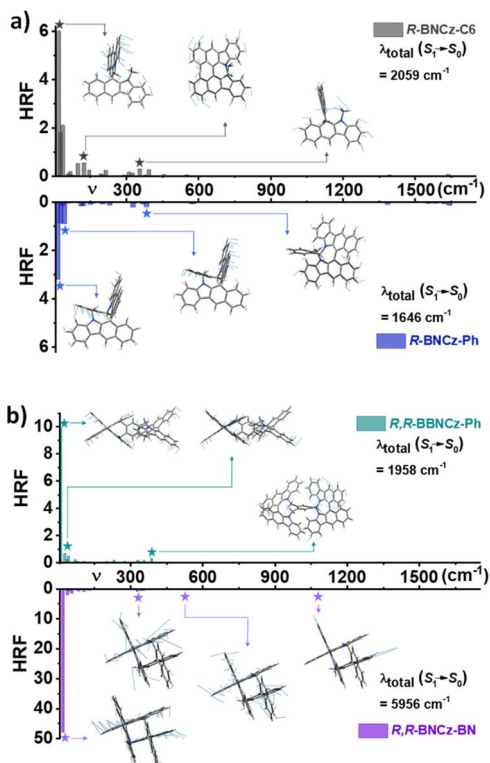


Fig. 4 The comparison of calculated HRFs versus frequencies during the  $S_1 \rightarrow S_0$  transition (inset: the predominant vibration modes of these molecules), (a) for **R-BNCz-C6** and **R-BNCz-Ph**, and (b) for **R,R-BBNCz-Ph** and **R,R-BNCz-BN**.

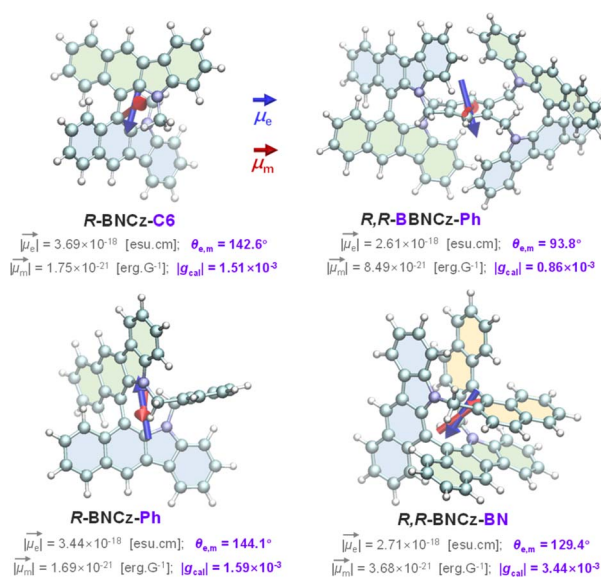


Fig. 5 Calculated key CPPL parameters involved in the  $S_1 \rightarrow S_0$  transition.

the others, showing threefold amplified  $g_{\text{PL}}$  values up to  $3.0 \times 10^{-3}$ . This enhancement might be attributed to the contribution of intermolecular chiral–chiral interactions in the highly doped thin films (20 wt%).

To fully understand the diversity of photophysical properties, density functional theory (DFT) calculations were executed for independent molecules using the Gaussian 16 software package. For brevity, all alkyl chains were simplified as methyl groups, and only right-hand (*R*) models were included. As expected, the highest occupied molecular orbitals (HOMO) and lowest unoccupied molecular orbitals (LUMO) of these chiral models were predominantly distributed on the BNCz backbones, exhibiting typical  $\pi$ -bonding characteristics (Fig. S16†). In addition, a significant proportion of HOMOs were located on the electron-rich nitrogen atoms and extended to the *ortho/para* positions of the conjugated carbon atoms, while LUMOs were confined to the electron-deficient carbon atoms at the *meta*-position of nitrogen, resulting in partially SR-CT participated excited states. Natural transition orbital (NTO) analysis confirmed the hybrid charge-transfer characteristics of the  $S_1 \rightarrow S_0$  transition (Fig. 3), especially for **R-BNCz-Ph** (Fig. 3b), which facilitated enhancements in both spin-orbital coupling (SOC) values between different excited states with different spin multiplicities, and oscillator strength ( $f$ ) between excited states and ground states. Notably, the calculated SOC matrix element  $\langle S_1 | \hat{H}_{\text{SOC}} | T_1 \rangle$  value for **R-BNCz-Ph** was nearly double ( $0.456 \text{ cm}^{-1}$ ) that of the primary **R-BNCz-C6** ( $0.269 \text{ cm}^{-1}$ ), together with an enhanced  $f$  from 0.081 to 0.108, attributed to the increased hybrid ratios of SR-CT in the excited states of the latter than the former. Additionally, for **R,R-BBNCz-Ph**, with a duplicate chromophore and  $C_2$ -symmetry, denser and more mixed excited states for interorbital coupling contributed to a further promoted SOC matrix element  $\langle S_1 | \hat{H}_{\text{SOC}} | T_2 \rangle$  value of up to  $0.935 \text{ cm}^{-1}$ .

The vibrational relaxation during the excitation and radiative transition processes was investigated based on the optimized geometrical configurations of  $S_1$  and  $S_0$ . Compared to the nonrestrictive **R-BNCz-C6**, the 3D-interlocked structure enabled a more rigid and stable architecture, with calculated root-mean-square deviations (RMSDs) decreasing from 0.286 to 0.153 Å. The Huang–Rhys factors (HRFs) associated with different vibrational modes during the  $S_1 \rightarrow S_0$  process were systematically simulated and analyzed using the Molecular Materials Property Prediction Package (MOMAP, Fig. 4).<sup>17</sup> Both **R-BNCz-C6** and **R-BNCz-Ph** demonstrated relatively large HRFs at low-frequency regions, attributed to the out-of-plane bending and swing of the BNCz plane. Compared to **R-BNCz-C6**, the calculated HRFs and total reorganization energies ( $\lambda_{\text{total}}$ ) for **R-BNCz-Ph** were significantly reduced, implying improved molecular rigidity *via* 3D-interlocking (Fig. 4a). With the incorporation of two identical BNCz chiral centers (**R,R-BBNCz-Ph**), more vibrational modes were predictably involved in the chiral chromophore, resulting in a slight increase in  $\lambda_{\text{total}}$  to  $1958 \text{ cm}^{-1}$  (Fig. 4b). For **R,R-BNCz-BN**, the presence of two orthogonal chiral centers, combined with significant through-space  $\pi$ – $\pi$  interactions ( $\sim 2.91 \text{ Å}$ ), likely induced additional vibrational modes and intramolecular repulsive forces, consequently leading to a substantial increase in the  $\lambda_{\text{total}}$  value.<sup>18</sup> To further elucidate the variation in chiroptical properties due to incremental changes in molecular parameters, theoretical simulations were conducted at the PBE0/Def2-SVP level using the TD-DFT method, providing critical parameters such as magnetic ( $\mu_m$ ) and electric dipole moments ( $\mu_e$ ), along with the

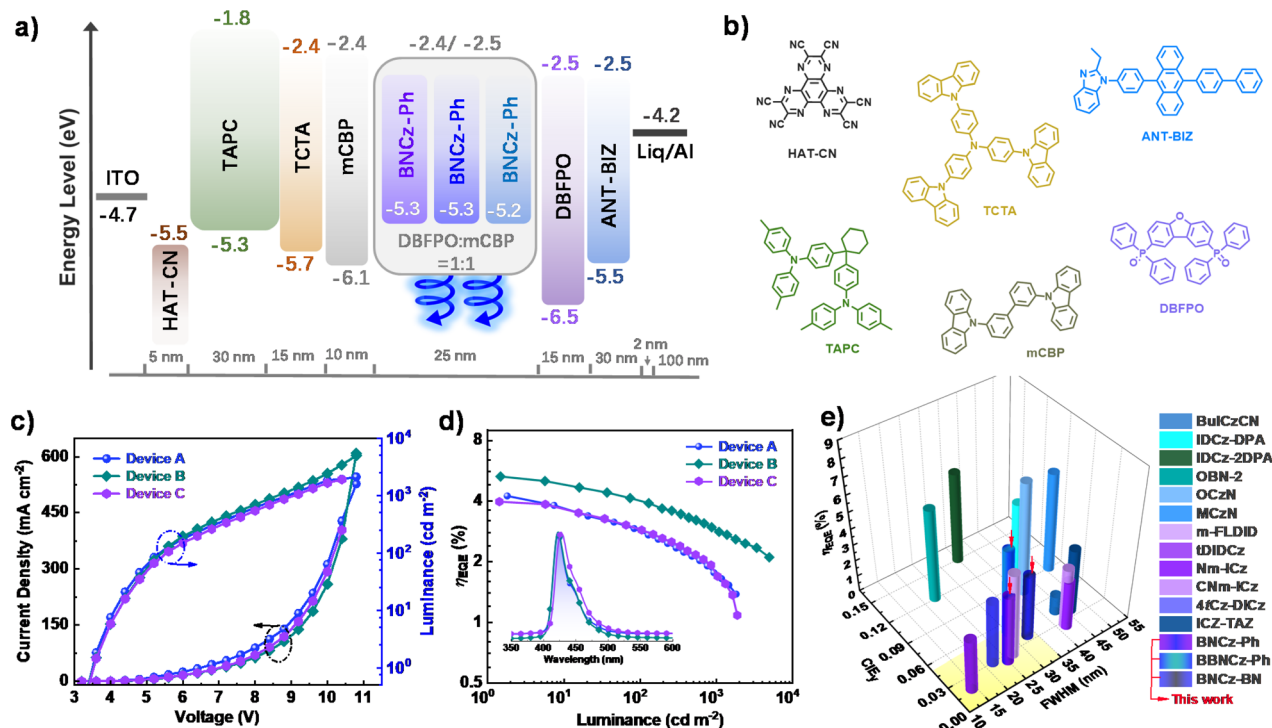


Fig. 6 (a) Schematic illustration of the device architectures and associated energy levels of the constituent materials, (b) the chemical structure of these used materials, (c) the  $J$ - $V$ - $L$  curves and (d) the  $\eta_{\text{EQE}}$  versus luminance (inset: EL spectra at 6 V) of these devices. (e) Multi-dimensional parallel comparison (involving CIE<sub>y</sub>, FWHM, and  $\eta_{\text{EQE,max}}$ ) of the EL performances for MR type blue fluorescence emitters based OLEDs (with  $\text{EL}_{\text{peak}} > 400 \text{ nm}$ ).

corresponding transition angles ( $\theta_{\text{e,m}}$ ) during the  $S_1 \rightarrow S_0$  transition (Fig. 5). Despite both **R-BNCz-C6** and **R-BNCz-Ph** exhibited similar calculated CPPL parameters, with  $g$  factors ( $g_{\text{cal}}$ ) around  $1.5 \times 10^{-3}$ , consistent with results measured in dilute toluene ( $1.1 \times 10^{-3}$ ). Actually, the observed CPPL signal for **R-BNCz-C6** was nearly negligible, which can be attributed to the flexible skeleton leading to uncertain or countervailing CPPL signals (Fig. S18<sup>†</sup>),<sup>15a</sup> underscoring the significance of 3D-interlocking strategy. With the incorporation of a secondary chiral center, the calculated  $\theta_{\text{e,m}}$  values split into two opposite directions depending on molecular symmetry. Specifically, two different chiral chromophores with mutually orthogonal configurations (**R,R-BNCz-BN**) yielded a favorable  $\theta_{\text{e,m}}$  of 129.4°, while two identical chiral motifs with  $C_2$ -symmetry (**R,R-BBNCz-Ph**) delivered an almost vertical angle of 93.8°. Consequently, distinct  $g_{\text{cal}}$  values of  $0.86 \times 10^{-3}$  and  $3.44 \times 10^{-3}$  were obtained for **R,R-BBNCz-Ph** and **R,R-BNCz-BN**, respectively, suggesting that the incorporation of a suitably positioned secondary chiral

center in close proximity to the primary one can effectively reinforce potential chiral-chiral interactions.

To evaluate the potential application in CP-OLEDs, vacuum-deposited electroluminescence devices incorporating these chiral compounds as emitting layers were prepared, with the detail configuration of “ITO/HAT-CN (5 nm)/TAPC (30 nm)/TCTA (15 nm)/mCBP (10 nm)/emitting layers (25 nm)/DBFPO (15 nm)/ANT-BIZ (30 nm)/Liq (2 nm)/Al (100 nm)”. The emitting layer composed of **R-BNCz-Ph**, **R,R-BBNCz-Ph** or **R,R-BNCz-BN** (20 wt% doped in DBFPO : mCBP blended matrix, 1 : 1) were designated as device A, B or C, respectively (Fig. 6a and b). Notably, all devices demonstrated pure deep-blue emission with CIE<sub>y</sub> < 0.05, and no residual peak from the hybrid host was observed under any bias, indicating an efficient host-dopant energy transfer channel. The FWHM of **R-BNCz-Ph**, **R,R-BBNCz-Ph** and **R,R-BNCz-BN** based devices were slightly broadened to 25, 30 and 33 nm, respectively, compared to the results in toluene (Fig. 6d). Due to the small FWHM and

Table 2 EL performance of these chiral emitters based devices

Device codes (emitters)	$V_{\text{on}}^a$ [V]	$L_{\text{max}}^b$ [cd m <sup>-2</sup> ]	$\eta_{\text{c,max}}^c$ [cd A <sup>-1</sup> ]	$\eta_{\text{p,max}}^c$ [lm W <sup>-1</sup> ]	$\eta_{\text{EQE,max}}^c$ [%]	$\text{EL}_{\text{peak}}^d$ [nm]	FWHM <sup>d</sup> [nm]	CIE <sup>d</sup> [x, y]
A (S-BNCz-Ph)	3.6	2104	1.07	0.94	4.23	423	25	0.157, 0.024
B (S,S-BBNCz-Ph)	3.6	4975	2.69	2.64	5.35	423	30	0.166, 0.049
C (S,S-BNCz-BN)	3.6	1898	1.38	1.21	4.00	427	33	0.158, 0.036

<sup>a</sup> Turn-on voltage at the luminance of 1 cd m<sup>-2</sup>. <sup>b</sup> The maximum brightness of the devices. <sup>c</sup> The  $\eta_{\text{c,max}}$ ,  $\eta_{\text{p,max}}$  and  $\eta_{\text{EQE,max}}$  values of these devices.

<sup>d</sup> The electroluminescent emission peaks, FWHM, and CIE coordinates of these devices under the unified bias of 6 V.



satisfactory emission peaks (423–427 nm), all the devices achieved desirable CIE coordinates aligning with the BT.2020 standard for pure-blue emitters. For example, under the same bias of 6 V, CIE coordinates of (0.157, 0.024) for device A, (0.166, 0.049) for device B, and (0.158, 0.036) for device C were realized. As revealed in Fig. 6d and Table 2, the maximum external quantum efficiency ( $\eta_{\text{EQE,max}}$ ) of these devices all exceeded 4.00%, with the highest value reaching 5.35% (device B), which surpasses the theoretical limits of traditional fluorescence-based OLEDs. In addition, the EL performances of **R,R-BBNCz-Ph**-based device, with the maximum current efficiency ( $\eta_{\text{c,max}}$ ) of 2.69 cd A<sup>-1</sup> and power efficiency ( $\eta_{\text{EQE,max}}$ ) of 2.64 lm W<sup>-1</sup>, were significantly better than those of the other two, which could be ascribed to the higher PLQY and more favorable horizontal transition dipole orientation of the former compared to the latter two (Fig. 5 and S17†). Nevertheless, all three devices demonstrated very competitive results, delivering some of the optimal values among blue fluorescence emitter-based OLEDs, particularly in the extreme blue region with CIE<sub>y</sub> < 0.05 and FWHM < 35 nm (Fig. 6e and Table S1†).

## Conclusions

In summary, four pairs of novel chiral emitters, with systematically varied molecular rigidity, symmetry, and chiral centers, were meticulously designed and synthesized. Photophysical measurements and theoretical calculations underscored the efficacy of enhancing both chiroptical activity and luminous efficiency of the axial chirality skeleton by incorporating intramolecular 3D-interlocking. Additionally, introducing a secondary chiral center closely parallel to the primary chiral plane facilitated strong chiral–chiral interactions, further improving their  $g_{\text{PL}}$  values. Notably, all these rigid 3D-interlocked chiral emitters exhibited bright deep-blue emission, with significantly narrowed FWHM as low as 18 nm and markedly improved  $g_{\text{PL}}$  values up to  $1.6 \times 10^{-3}$ , which could be further amplified to approximately  $3.0 \times 10^{-3}$  in doped thin films. Vacuum-deposited CP-OLEDs incorporating these emitters showcased outstanding electroluminescent performance, with  $\eta_{\text{EQE,max}}$  exceeding 5%, favorable FWHM of approximately 25 nm, and extreme CIE<sub>y</sub> < 0.03, positioning them among the optimal values for blue fluorescence emitter-based OLEDs. Our findings not only provide deep insights into the key parameters for achieving strong chiroptical activity, concerning molecular symmetry, configurational stability, and secondary chiral centers, but also propose an effective strategy for generating desirable CPL emitters for state-of-the-art CP-OLEDs.

## Data availability

The data that support the findings of this study are available from the corresponding author upon reasonable request.

## Author contributions

X. Mo, materials synthesis, investigation and writing-original draft, Y. Li, X. Chen and B. Xiao support the materials

preparation and measurements, G. Chen carry out the OLED assessment, X. Yin provide the initial conception, CPL measurements, DFT calculations, analysis, and writing-review & editing, C. Yang undertake supervision, and proofreading this manuscript.

## Conflicts of interest

There are no conflicts to declare.

## Acknowledgements

This research was financially supported by the Natural Science Foundation of Guangdong Province (Project No. 2023A1515030125 and 2024A1515010744), and the Shenzhen Science and Technology Program (No. JCYJ20220818095816036 and 20220810131017001). The authors thank Kui Gong, Yibin Hu, and Yin Wang (all from HZWTECH) for help and discussions regarding this study. The authors also thank the Instrumental Analysis Center of Shenzhen University for Analytical Support.

## Notes and references

- (a) S. Yang, S. Zhang, F. Hu, J. Han and F. Li, *Coord. Chem. Rev.*, 2023, **485**, 215116; (b) X. Wu, J. W. Huang, B. K. Su, S. Wang, L. Yuan, W. Q. Zheng, H. Zhang, Y. X. Zheng, W. Zhu and P. T. Chou, *Adv. Mater.*, 2022, **34**, 2105080; (c) F. Zhang, F. Rauch, A. Swain, T. B. Marder and P. Ravat, *Angew. Chem. Int. Ed. Engl.*, 2023, **62**, e202218965.
- (a) C. Zhang, S. Li, X. Y. Dong and S. Q. Zang, *Aggregate*, 2021, **2**, e48; (b) Y. Li, Z. Zhang, T. Li, Y. Liang, W. Si and Y. Lin, *Angew. Chem., Int. Ed.*, 2023, **62**, e202307466.
- G. Long, R. Sabatini, M. I. Saidaminov, G. Lakhwani, A. Rasmita, X. Liu, E. H. Sargent and W. Gao, *Nat. Rev. Mater.*, 2020, **5**, 423–439.
- I. Song, J. Ahn, H. Ahn, S. H. Lee, J. Mei, N. A. Kotov and J. H. Oh, *Nature*, 2023, **617**, 92–99.
- (a) L. Yuan, J. W. Xu, Z. P. Yan, Y. F. Yang, D. Mao, J. J. Hu, H. X. Ni, C. H. Li, J. L. Zuo and Y. X. Zheng, *Angew. Chem., Int. Ed.*, 2024, **63**, e202407277; (b) Q. Dong, B. He, W. Qiao, W. Zhu, P. Duan and Y. Wang, *Chem. Commun.*, 2024, **60**, 3421–3424; (c) L. Xu, H. Liu, X. Peng, P. Shen, B. Z. Tang and Z. Zhao, *Angew. Chem. Int. Ed. Engl.*, 2023, **62**, e202300492.
- (a) A. M. T. Muthig, O. Mrozek, T. Ferschke, M. Rodel, B. Ewald, J. Kuhnt, C. Lenczyk, J. Pflaum and A. Steffen, *J. Am. Chem. Soc.*, 2023, **145**, 4438–4449; (b) P. Li, W. Li, Q. Lv, R. Chen and C. Zheng, *J. Mater. Chem. C*, 2023, **11**, 4033–4041; (c) L. Frédéric, A. Desmarchelier, L. Favereau and G. Pieters, *Adv. Funct. Mater.*, 2021, **31**, 2010281; (d) W. R. Kitzmann, J. Freudenthal, A.-P. M. Reponen, Z. A. VanOrman and S. Feldmann, *Adv. Mater.*, 2023, **35**, 2302279; (e) Z. Chen, M. Huang, C. Zhong, S. Gong, V. Coropceanu, J.-L. Brédas and C. Yang, *Chem. Sci.*, 2023, **14**, 6022–6031.



- 7 (a) S.-Q. Song, X. Han, Z.-Z. Huo, C.-F. Yip, X.-F. Hong, M.-N. Ding and Y.-X. Zheng, *Sci. China: Chem.*, 2024, **67**, 2257–2264; (b) J. L. Greenfield, J. Wade, J. R. Brandt, X. Shi, T. J. Penfold and M. J. Fuchter, *Chem. Sci.*, 2021, **12**, 8589–8602; (c) J. Crassous, M. J. Fuchter, D. E. Freedman, N. A. Kotov, J. Moon, M. C. Beard and S. Feldmann, *Nat. Rev. Mater.*, 2023, **8**, 365–371.
- 8 (a) K.-K. Tan, W.-C. Guo, W.-L. Zhao, M. Li and C.-F. Chen, *Angew. Chem., Int. Ed.*, 2024, **63**, e202412283; (b) Y. Xue, C. Zhang, T. Lv, L. Qiu and F. Wang, *Angew. Chem., Int. Ed.*, 2023, **62**, e202300972; (c) D. W. Zhang, M. Li and C. F. Chen, *Angew. Chem. Int. Ed. Engl.*, 2022, **61**, e202213130; (d) K. Velmurugan, A. Murtaza, A. Saeed, J. Li, K. Wang, M. Zuo, Q. Liu and X.-Y. Hu, *CCS Chem.*, 2022, **4**, 3426–3439; (e) Z. Geng, Y. Zhang, Y. Zhang, Y. Quan and Y. Cheng, *Angew. Chem., Int. Ed.*, 2022, **61**, e202202718.
- 9 (a) Y. Zhang, Y. Li, Y. Quan, S. Ye and Y. Cheng, *Angew. Chem. Int. Ed. Engl.*, 2023, **62**, e202214424; (b) Y. Wang, R. Liu, Z. Zhang, J. Wei and Z. Yang, *J. Am. Chem. Soc.*, 2023, **145**, 4035–4044; (c) J. Hong, S. Kim, G. Park, Y. Lee, H. Kim, S. Kim, T. W. Lee, C. Kim and Y. You, *Chem. Sci.*, 2021, **12**, 8668–8681.
- 10 (a) Z. Ye, H. Wu, Y. Xu, T. Hua, G. Chen, Z. Chen, X. Yin, M. Huang, K. Xu, X. Song, Z. Huang, X. Lv, J. Miao, X. Cao and C. Yang, *Adv. Mater.*, 2024, **36**, 2308314; (b) Y. F. Wu, S. W. Ying, L. Y. Su, J. J. Du, L. Zhang, B. W. Chen, H. R. Tian, H. Xu, M. L. Zhang, X. Yan, Q. Zhang, S. Y. Xie and L. S. Zheng, *J. Am. Chem. Soc.*, 2022, **144**, 10736–10742; (c) F. Gan, G. Zhang, J. Liang, C. Shen and H. Qiu, *Angew. Chem., Int. Ed.*, 2024, **63**, e202320076.
- 11 (a) Q. Wang, L. Yuan, C. Qu, T. Huang, X. Song, Y. Xu, Y. X. Zheng and Y. Wang, *Adv. Mater.*, 2023, **35**, 2305125; (b) W. Yang, N. Li, J. Miao, L. Zhan, S. Gong, Z. Huang and C. Yang, *CCS Chem.*, 2022, **4**, 3463–3471; (c) J. M. dos Santos, D. Sun, J. M. Moreno-Naranjo, D. Hall, F. Zinna, S. T. J. Ryan, W. Shi, T. Matulaitis, D. B. Cordes, A. M. Z. Slawin, D. Beljonne, S. L. Warriner, Y. Olivier, M. J. Fuchter and E. Zysman-Colman, *J. Mater. Chem. C*, 2022, **10**, 4861–4870; (d) X. Xiao, S. K. Pedersen, D. Aranda, J. Yang, R. A. Wiscons, M. Pittelkow, M. L. Steigerwald, F. Santoro, N. J. Schuster and C. Nuckolls, *J. Am. Chem. Soc.*, 2021, **143**, 983–991.
- 12 (a) F. Furlan, J. M. Moreno-Naranjo, N. Gasparini, S. Feldmann, J. Wade and M. J. Fuchter, *Nat. Photonics*, 2024, **18**, 658–668; (b) D. Ayuso, O. Neufeld, A. F. Ordonez, P. Decleva, G. Lerner, O. Cohen, M. Ivanov and O. Smirnova, *Nat. Photonics*, 2019, **13**, 866–871.
- 13 (a) Z. P. Yan, L. Yuan, Y. Zhang, M. X. Mao, X. J. Liao, H. X. Ni, Z. H. Wang, Z. An, Y. X. Zheng and J. L. Zuo, *Adv. Mater.*, 2022, **34**, 2204253; (b) F. C. Kong, S. Y. Yang, X. J. Liao, Z. Q. Feng, W. S. Shen, Z. Q. Jiang, D. Y. Zhou, Y. X. Zheng and L. S. Liao, *Adv. Funct. Mater.*, 2022, **32**, 2201512; (c) Z. P. Yan, T. T. Liu, R. Wu, X. Liang, Z. Q. Li, L. Zhou, Y. X. Zheng and J. L. Zuo, *Adv. Funct. Mater.*, 2021, **31**, 2103875; (d) S.-P. Wan, H.-Y. Lu, M. Li and C.-F. Chen, *J. Photochem. Photobiol., C*, 2022, **50**, 100500.
- 14 J. M. Teng and C. F. Chen, *Adv. Opt. Mater.*, 2023, **11**, 2300550.
- 15 (a) X. Yin, H. Huang, N. Li, W. Li, X. Mo, M. Huang, G. Chen, J. Miao and C. Yang, *Mater. Horiz.*, 2024, **11**, 1752–1759; (b) H. Huang, N. Li, W. Li, X. Mo, X. Cao, J. Miao, X. Yin and C. Yang, *Adv. Funct. Mater.*, 2024, **34**, 2403191.
- 16 (a) Y. Wei, C. Zhong, Y. Sun, S. Ma, M. Ni, X. Wu, Y. Yan, L. Yang, I. A. Khodov, J. Ge, Y. Li, D. Lin, Y. Wang, Q. Bao, H. Zhang, S. Wang, J. Song, J. Lin, L. Xie and W. Huang, *Nat. Commun.*, 2024, **15**, 5438; (b) Z. Song, H. Sato, A. Pietropaolo, Q. Wang, S. Shimoda, H. Dai, Y. Imai, H. Toda, T. Harada, Y. Shichibu, K. Konishi, M. Bando, N. Naga and T. Nakano, *Chem. Commun.*, 2022, **58**, 1029–1032; (c) J. Chen, H. Liu, J. Guo, J. Wang, N. Qiu, S. Xiao, J. Chi, D. Yang, D. Ma, Z. Zhao and B. Z. Tang, *Angew. Chem. Int. Ed. Engl.*, 2022, **61**, e202116810; (d) K. Dhbaibi, L. Abella, S. Meunier-Della-Gatta, T. Roisnel, N. Vanthuyne, B. Jamoussi, G. Pieters, B. Racine, E. Quesnel, J. Autschbach, J. Crassous and L. Favereau, *Chem. Sci.*, 2021, **12**, 5522–5533.
- 17 (a) Z. Shuai and Q. Peng, *Natl. Sci. Rev.*, 2017, **4**, 224–239; (b) Z. Shuai and Q. Peng, *Phys. Rep.*, 2014, **537**, 123–156; (c) Z. Shuai, *Chin. J. Chem.*, 2020, **38**, 1223–1232.
- 18 (a) J. Fan, Y. Xu, N. Li, J. Miao, C. Zhou, T. Liu, M. Zhu and X. Yin, *J. Mater. Chem. C*, 2022, **10**, 17059–17065; (b) H. Huang, N. Li, S. Fu, X. Mo, X. Cao, X. Yin and C. Yang, *Adv. Sci.*, 2023, **10**, 2304204.

